Probing the flavor violating scalar top quark signal at the LHC

Genevieve Belanger,[1] Diptimoy Ghosh,[2] Rohini Godbole,[3] Monoranjan Guchait,[4] and Dipan Sengupta[4]

[1]*LAPTH, Université de Savoie, CNRS, B.P. 110, F-74941 Annecy-le-Vieux, France*
[2]*INFN, Sezione di Roma, Piazzale Aldo Moro 2, I-00185 Roma, Italy*
[3]*Center for High Energy Physics, Indian Institute of Science, Bangalore 560012, India*
[4]*Department of High Energy Physics, Tata Institute of Fundamental Research, 1, Homi Bhabha Road, Mumbai 400 005, India*

The Large Hadron Collider (LHC) has completed its run at 8 TeV with the experiments ATLAS and CMS having collected about 25 fb^{-1} of data each. Discovery of a light Higgs boson coupled with lack of evidence for supersymmetry at the LHC so far, has motivated studies of supersymmetry in the context of naturalness with the principal focus being the third generation squarks. In this work, we analyze the prospects of the flavor violating decay mode $\tilde{t}_1 \to c\chi_1^0$ at 8 and 13 TeV center-of-mass energy at the LHC. This channel is also relevant in the dark matter context for the stop-coannihilation scenario, where the relic density depends on the mass difference between the lighter stop quark ($\tilde{t}_1$) and the lightest neutralino (χ_1^0) states. This channel is extremely challenging to probe, especially for situations when the mass difference between the lighter stop quark and the lightest neutralino is small. Using certain kinematical properties of signal events we find that the level of backgrounds can be reduced substantially. We find that the prospect for this channel is limited due to the low production cross section for top squarks and limited luminosity at 8 TeV, but at the 13 TeV LHC with 100 fb^{-1} luminosity, it is possible to probe top squarks with masses up to $\sim$450 GeV. We also discuss how the sensitivity could be significantly improved by tagging charm jets.

I. INTRODUCTION

At the end of the 8 TeV run the Large Hadron Collider (LHC) has collected about 25 fb^{-1} of data and produced the most defining observation since the onset of its operation in 2008. This observation is the finding of a new boson at 125 GeV [1,2], which in all its glory seems to behave like the standard model (SM) Higgs boson. However, its true nature will be revealed only after precision measurements of its couplings and spin as well as their comparison with SM predictions. Interestingly, this discovery of the Higgs-like boson has galvanized the beyond standard model (BSM) physics hunters in analyzing its impact on various new physics models including supersymmetry (SUSY). The implications of the 125 GeV Higgs on SUSY have been well studied in the literature [3–34] and this is sure to continue in the coming days.

The early searches in SUSY, the most popular model among all the BSM options, have focused, both phenomenologically [35–38] and experimentally [39,40] on the constrained minimal supersymmetric standard model (CMSSM)/minimal supergravity [41–46]. The initial searches probed mainly the gluino ($\tilde{g}$) and the squarks ($\tilde{q}$) of the first two generations. The current lower limits on the gluino and the first two generations squark masses in the framework of CMSSM stand at $m_{\tilde{g}} > 1.5$ TeV for almost degenerate gluino and squarks and $m_{\tilde{q}} > 1.4$ TeV for very high squark masses [47–49]. The LHC constraints on the third generation squarks, stops ($\tilde{t}_{1,2}$) and sbottoms ($\tilde{b}_{1,2}$) are weaker because of

the lower production cross section for a squark pair of a single flavor and are weakened even further when the mass difference between the squark and the neutralino is small. The negative results in the initial searches for the gluino and first two generations of squarks, together with the discovery of a "light" Higgs boson have prompted consideration of natural SUSY, and hence a light third generation squark as an attractive framework for phenomenological studies.

Natural SUSY [10,18,50–55] is inspired by the observation that the most relevant superparticles responsible for cancellation of quadratic divergences in the Higgs loop corrections are stop quarks. At the loop level the Higgs potential receives corrections from gauge and Yukawa interactions, the dominant part being the top-stop loop. The radiative corrections ($\delta m_{H_u}^2$) are quadratically proportional to the third generation left and right soft masses along with the trilinear coupling A_t. Thus the trilinear couplings and the soft masses which control the third generation spectrum determine the level of fine-tuning required to stabilize the Higgs mass in the theory. Another measure of " naturalness" is also inspired by demanding that the level of fine-tuning among different terms in the relation connecting M_Z^2, μ^2 and the SUSY breaking scale is not high. These considerations thus imply light Higgsinos or light third generation squarks. The natural SUSY spectrum thus requires only a few particles below the TeV scale, the stops and the sbottom, the lighter charginos and neutralinos, and the gluino [10,54–56]. These natural SUSY scenarios have been studied in the literature for a wide range of

phenomenological models and signatures. Furthermore, the anatomy of lighter third generation superparticles has been well dissected in the literature in terms of models and collider signatures [51,52,57–79].

Most of these studies, especially in the context of colliders, have focused on the decay of lighter stop ($\tilde{t}_1$) and bottom ($\tilde{b}_1$), $\tilde{t}_1 \rightarrow t\chi_1^0$ and $\tilde{b}_1 \rightarrow b\chi_1^0$ respectively. It has been observed that the feasibility of these channels depend critically on the mass difference

$$\Delta m = m_{\tilde{t}_1(\tilde{b}_1)} - m_{\chi_1^0}, \tag{1}$$

since it determines the hardness of the final state particles. A large value of Δm leads to large jet momentum and a sizable missing transverse momentum ($\not{p}_T$), both of which are imperative to suppress the SM backgrounds. Interestingly in the large Δm scenario, the use of jet substructure and top tagging is also an important tool to suppress backgrounds [80,81]. To alleviate the problem of low mass differences, shape analysis with various kinematic variables have also been considered [71].

As noted earlier the nonobservation of a light sparticle in a strongly interacting sector, i.e., a gluino and/or a squark of first two generations, in the sub-TeV regime along with the observation of a light Higgs have prompted ATLAS and CMS to perform dedicated searches for the third generations squarks. Note that, the limits on the masses of the squarks of the first two generations using the generic SUSY searches are not applicable to the case of the third generation squarks. The dedicated searches look for third generation squarks produced directly via QCD processes as well as those produced indirectly in gluino decays, in a plethora of final states coming from a variety of decay channels of $\tilde{t}_1$ assuming specific mass relationships among $\tilde{g}$, $\tilde{t}_1$, $\chi_1^\pm$ and the χ_1^0 assumed to be the lightest SUSY particle (LSP). The principle decay channels studied are $\tilde{t}_1 \rightarrow t\chi_1^0$ and $\tilde{t}_1 \rightarrow b\chi_1^\pm$, with leptons and b jets in the final state from top quark decay. ATLAS searched for $\tilde{t}_1$ in the decay channel, $\tilde{t}_1 \rightarrow t\chi_1^0$, from direct stop pair production using 8 TeV LHC data with 13 fb^{-1} luminosity and ruled out $m_{\tilde{t}_1}$ between 225 and 575 GeV for a LSP mass up to 175 GeV [82]. ATLAS also probed $\tilde{t}_1$ in the channel $\tilde{t}_1 \rightarrow b\chi_1^\pm \rightarrow b\chi_1^0 f f'$ assuming $\Delta m = m_{\chi_1^\pm} - m_{\chi_1^0}$ to be 5 and 20 GeV. For $\Delta m = 5$ GeV they ruled out stop masses of about 600 GeV in a corridor of lightest neutralino mass [83]. With the use of the kinematic variable M$_{T2}$, ATLAS also excluded $m_{\tilde{t}_1}$ in the range of 150–450 GeV for the channel $\tilde{t}_1 \rightarrow b\chi_1^\pm$, where the chargino is nearly degenerate with the $\tilde{t}_1$ state [84]. Similarly, CMS searched for $\tilde{t}_1$ in the channels $\tilde{t}_1 \rightarrow t\chi_1^0$ and $\tilde{t}_1 \rightarrow b\chi_1^\pm$, and excluded it with a mass between 160 and 430 GeV for a LSP mass up to 150 GeV [85].

However, when the lighter stop becomes the next-to-lightest SUSY particle (NLSP), the stop searches at colliders are quite different and become challenging. In this scenario, the dominant decay modes are via the flavor changing decays and the four body decay [86–88],

$$\tilde{t}_1 \rightarrow c\chi_1^0 \tag{2}$$
$$\rightarrow b f f' \chi_1^0. \tag{3}$$

Stop pair production followed by these decays leads to final states containing a heavy quark pair $c\bar{c}$ or $b\bar{b}$ respectively and are given by

$$pp \rightarrow \tilde{t}_1 \tilde{t}_1^* \rightarrow c\bar{c} + 2\chi_1^0 \rightarrow 2 \text{ jets} + \not{p}_T, \tag{4}$$

$$pp \rightarrow \tilde{t}_1 \tilde{t}_1^* \rightarrow b\bar{b} + 2\chi_1^0 + 2f f'. \tag{5}$$

The flavor violating decay mode yields precisely two jets and missing transverse momenta ($\not{p}_T$) due to the presence of χ_1^0. The relative decay rates into the above two channels are extremely sensitive to the model parameters [88,89]. The signal sensitivity for the four body decay channels has been studied for different parameters [90].

For very low values of Δm [Eq. (1)] it is rather difficult to obtain a reasonable signal sensitivity. In this case, the strategies have been to look at the monojet $+\not{p}_T$ [58,59] and monophoton $+\not{p}_T$ final state [91,92]. The experimental limits on these channels come from reinterpretation of the monojet searches in ATLAS and CMS [93,94]. With the available data at 7 TeV, lighter stops of mass below about 200 GeV are excluded for the above-mentioned decay channels. Thus the limits on the mass of the lightest stop from these channels are rather weak. This is because the final state objects are soft due to the low value of Δm leading to a lower acceptance of signal events. Therefore, it is a challenging task to probe these channels for very low Δm cases.

In this work we explore the possibility to find a signal for $\tilde{t}_1$ in the flavor violating decay Eq. (4) resulting in a dijet $+\not{p}_T$ signature. Note that the flavor violating decay mode is also important in the dark matter context in the stop-coannihilation scenario [88]. The correct relic density abundance in this case crucially depends on Δm. In analyzing this signal we apply different types of kinematic selection cuts which are described in the following sections. For the case of the flavor violating decay mode, the presence of c quarks can be exploited by tagging c jets. It is known that tagging c jets is not easy because of the low mass of c quark and the low decay length of the charmed mesons. However, the development of a strategy to tag the c jets, even with a modest efficiency will be helpful to suppress the SM backgrounds by an enormous amount and hence needs to be pursued.

The paper is organized as follows. In Sec. II a brief description of the parameter space of interest is discussed, while in Secs. III and IV we discuss our collider strategy and results respectively along with a discussion on the stop-coannihilation dark matter scenario. Finally we conclude in Sec. V.

II. PARAMETER SPACE

A. CMSSM and pMSSM

We simulate the signal [Eq. (4)] for the parameter space of our interest in the context of both CMSSM and the phenomenological MSSM (pMSSM) with 19 parameters [95]. The CMSSM has been the most popular model of SUSY breaking in the context of collider phenomenology and experimental searches over the last two decades. This is primarily driven by the economy of the model which requires four parameters and a sign, as compared to the cornucopia of over 100 parameters in the MSSM. These parameters defined at the grand unified theory (GUT) scale include the universal scalar mass (m_0), the universal fermion mass ($m_{1/2}$) and the universal trilinear coupling A_0, along with $\tan \beta$, the ratio of vacuum expectation values of the two Higgs doublets and the sign of μ, the Higgsino mass parameter, at the weak scale. The sparticle spectrum at the electroweak scale is obtained by renormalization group running from the GUT scale to the electroweak scale.

It is a well-known fact the Higgs mass receives a substantial quantum correction resulting in an enhancement of its mass from its tree-level values which is bounded by mass of Z boson, viz., $M_H^2 \leq M_Z^2 \cos^2 2\beta$. In order to accommodate the Higgs mass of 125 GeV in the CMSSM framework one necessarily requires stops in the multi-TeV regime or lighter stops with maximal mixing scenarios. Loop corrections can increase the tree-level Higgs mass up to $\sim$140 GeV 140 GeV, due to stop-top loops and a large value of the trilinear coupling A_t [3,4]. However it has also been noted that such large trilinear coupling introduces a significant amount of fine-tuning in the theory. On the other hand a large A_0 results in a large splitting in the stop mass matrix. This means that lighter stops are accessible at LHC energies even in CMSSM [4]. Hence it is worth investigating, in the CMSSM, the available parameter space, which provides $m_H \simeq 125$ GeV and where we have imposed various experimental and theoretical constraints as described below.

B. Constraining CMSSM

With this goal, we perform a numerical scan of the relevant part of the CMSSM parameter space, varying the range of parameters such as,

$$m_0: [0 \, 3 \text{ TeV}], \quad m_{1/2}: [0 \, 1 \text{ TeV}], \quad A_0: [-2 \, 10 \text{ TeV}],$$
$$(6)$$

and setting the top quark mass to be 172.9 GeV. We generate 5×10^5 random parameter points for a fixed value of $\tan \beta$. We fix the sign of the Higgsino mass parameter μ to be positive. We use the SuSpect [96] spectrum generator to generate the masses of the supersymmetric particles for a fixed set of input parameters along with SuperIso [97] for the calculations of the branching ratios of rare B-meson decays.

We refer to a point in the CMSSM parameter space to be allowed if it survives the following constraints:

(i) The lightest Higgs boson mass M_H falls in the window 122.5 GeV $< M_H <$ 129.5 GeV. Note that, owing to the small difference in the central values given by the AT-LAS and CMS collaborations [1,2], in order to be conservative, we used the number 126 ± 2 GeV as the experimental value. In addition, we added a 1.5 GeV theoretical uncertainty following [29].

(ii) The branching ratio ($\mathcal{B}$) of the radiative decay $B \to X_s \gamma$ satisfies the following 95% C.L. bound [98]:

$$2.6 \times 10^{-4} < \mathcal{B}(B \to X_s \gamma) \quad < 4.5 \times 10^{-4}.$$

The HFAG average and the SM predictions for this branching ratio are given by $[3.55 \pm 0.24 \pm 0.09] \times 10^{-4}$ [99] and $[3.15 \pm 0.23] \times 10^{-4}$ [100] respectively. We obtained the above 95% C.L. bound after including the intrinsic MSSM uncertainty of 0.15×10^{-4} following the prescription given in [101].

(iii) The branching ratio of $B_s \to \mu^+ \mu^-$ [102,103] lies in the 95% C.L. allowed range

$$1.3 \times 10^{-9} < \mathcal{B}(B_s \to \mu^+ \mu^-) < 4.5 \times 10^{-9}.$$

In order to get the above range we used the CMS + LHCb average and SM predictions to be $[2.9 \pm 0.7] \times 10^{-9}$ [102,103] and $[3.56 \pm 0.18] \times 10^{-9}$ [100] respectively.

Figures 1 and 2 show the results of our numerical study.

If a point is allowed by all of the three constraints above then the point is plotted in magenta (dark grey). A point is green (pale grey) if it satisfies only the constraint (i) but none of the other two. Note that all the points [except the red (black) points in the $m_0 - m_{1/2}$ plane] have been checked to satisfy the requirements of electroweak symmetry breaking, electric and color neutral LSP, the LEP lower bounds on the masses and other theoretical consistencies e.g., absence of tachyonic states and so on. It is worth mentioning here that the impact of the measured Higgs mass on the parameter space is rather strong; the region with low values of m_0 and $m_{1/2}$ is completely ruled out by this single measurement (i). The absence of green points for $\tan \beta = 10$ shows that the bounds from (ii) and (iii) above are not strong enough to rule out any point which is not already disallowed by the Higgs mass. This situation changes gradually as we go towards larger $\tan \beta$ values as can be seen from Fig. 2. In Fig. 2 there are many (green) points which are allowed by the Higgs mass but disfavored by the flavor physics data, in particular (iii). This happens because of the strong dependence of the branching ratios of $B \to X_s \gamma$ and $B_s \to \mu^+ \mu^-$ on $\tan \beta$. In fact, the dominant Higgs contribution to these branching ratios are proportional to $(\tan \beta)^2$ [for $\mathcal{B}(B \to X_s \gamma)$] and $(\tan \beta)^6$ [for $\mathcal{B}(B_s \to \mu^+ \mu^-)$]. This $(\tan \beta)^6$ dependence removes all the points with $m_0 < 3000$ GeV and $m_{1/2} < 1000$ GeV for $\tan \beta = 50$, hence we do not show them here. We would also
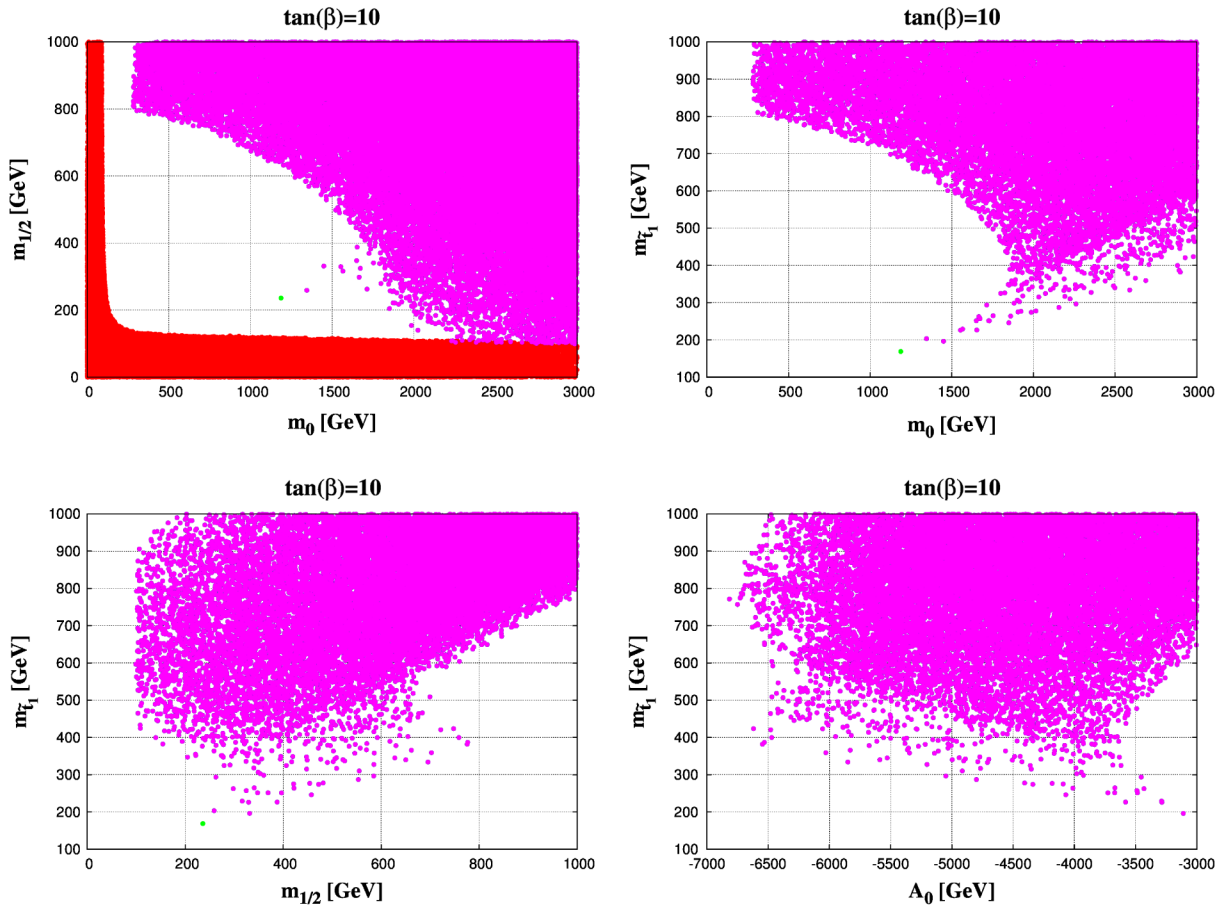
FIG. 1 (color online). The allowed parameter points in the $m_0 - m_{1/2}$ (top left panel), $m_0 - m_{\tilde{t}_1}$ (top right panel), $m_{1/2} - m_{\tilde{t}_1}$ (middle left panel), $A_0 - m_{\tilde{t}_1}$ (middle right panel), in the CMSSM scenario for $\tan\beta = 10$. The red (black) region in the top left panel corresponds to points that are theoretically inconsistent. All the three constraints mentioned in the text are satisfied for the magenta (dark grey) points, whereas for the green (pale grey) points only the Higgs mass constraint is satisfied but the B-physics constraints are not.

like to point out in passing that the dominant Higgs mediated diagrams mentioned above are also proportional to the stop trilinear coupling A_t. Thus the constraints from (ii) and (iii) can be relaxed for small values of A_t. On the other hand, the measured value of the Higgs mass prefers a large value of A_t. Hence, there is a complementarity between the bounds coming from the Higgs mass and those coming from the flavor physics data.

In both Figs. 1 and 2 we also show (in the second row) the allowed values of $m_{\tilde{t}_1}$ for a wide range of $m_{1/2}$ and A_0 values. In spite of the constraints discussed above, it is quite clear from these figures that even in the CMSSM, there exists regions in the parameter space where a light stop below a TeV mass scale is allowed.

C. Stop decay and benchmarks

While it is certainly interesting to find a large region of parameter space pertaining to lighter stops and allowed by the Higgs mass constraint, the specific mass relations in CMSSM tie our hands to a large extent. In the context of natural SUSY it is enough to consider only the third generation squarks (stops and sbottoms), and the third generation

trilinear couplings along with charginos and neutralinos. The rest of the spectrum is mostly unimportant and can be decoupled from this set. This rather simplified approach, in the framework of the pMSSM, brings out the relevant physics with the minimal number of input parameters.

The parameter space of our interest is guided by the region where the flavor violating decay $\tilde{t}_1 \to c\chi_1^0$ is kinematically dominant for relatively small mass differences corresponding to Eq. (1). The decay width is given by [86,87]

$$\Gamma = \frac{1}{2}\alpha|\epsilon|^2 m_{\tilde{t}_1}\left[1 - \frac{m_{\chi_1^0}^2}{m_{\tilde{t}_1}^2}\right]^2, \qquad (7)$$

where the loop factor ϵ is directly proportional to A_b^2 and $\tan^2\beta$ with α being the strong coupling constant.[1]

A competing decay mode to the two body is the four body decay $\tilde{t}_1 \to b\chi_1^0 f f'$ [86,87,89], dominantly via an off shell chargino into fermions. The two body decay mode, which is quadratically dependent on $\tan\beta$ and A_b dominates over the four body decay for moderate to high

---

[1]For an exact one-loop calculation of this decay width see [87].
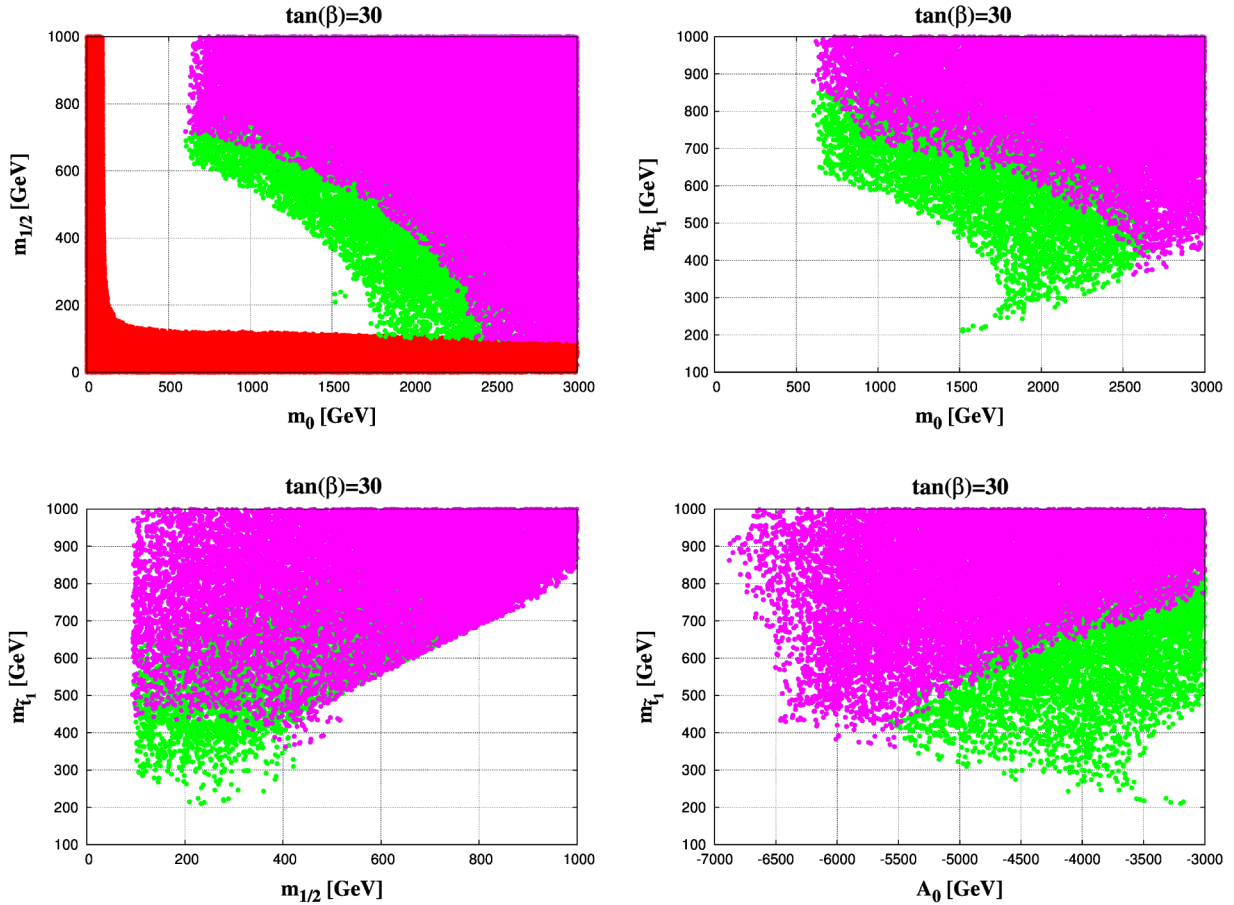
FIG. 2 (color online). The allowed parameter points in the $m_0 - m_{1/2}$ (top left panel), $m_0 - m_{\tilde{t}_1}$ (top right panel), $m_{1/2} - m_{\tilde{t}_1}$ (middle left panel), $A_0 - m_{\tilde{t}_1}$ (middle right panel), in the CMSSM scenario for $\tan\beta = 30$. The color code is the same as in Fig. 1.

$\tan\beta$. In the large $\tan\beta$ scenario, the two body decay mode dominates over the four body decay mode, for similar mass differences as compared to lower $\tan\beta$.

We choose two benchmark points in the CMSSM and four points in the 19-parameter pMSSM for our collider analysis. The representative points are shown in Tables I and II indicating the relevant branching ratios and other sparticle masses. All points in CMSSM (P1,P2) and three points in pMSSM (P3,P4,P5) are chosen to have $\tan\beta = 10$. We choose one additional benchmark point with $\tan\beta = 30$ in pMSSM (P6).

For the pMSSM benchmarks in Table II, we set the first two generations of squarks and all slepton generations to 5 TeV and the gluino to 1.5 TeV as they are irrelevant

TABLE I. Masses and branching ratios of some of the particles in the CMSSM scenario. All energy units in GeV. $\mathrm{sgn}(\mu)$ is set to be positive.

	$\tan\beta$	m_0	$m_{1/2}$	A_0	m_H	$m_{\tilde{t}_1}$	$m_{\chi_1^0}$	Δm	$BR(\tilde{t}_1 \to c\chi_1^0)$ %	$BR(\tilde{t}_1 \to bff'\chi_1^0)$ %
P1	10	1848	457.6	−4069	126.0	241	198	43	74	25
P2	10	2589	695	−5849	126	331	306	25	97	2

TABLE II. Masses of some of the sparticles for the benchmark points in the pMSSM scenario. In all cases, the remaining parameters are as described in the text. All energy units are in GeV.

	A_t	$\tan\beta$	μ	M_1	m_H	$m_{\tilde{Q}_3}$	$m_{\tilde{t}_R}$	$m_{\tilde{b}_R}$	$m_{\tilde{t}_1}$	$m_{\chi_1^0}$	Δm	$BR(\tilde{t}_1 \to c\chi_1^0)$ %	$BR(\tilde{t}_1 \to bff'\chi_1^0)$ %
P3	−1900	10	800	280	123.0	380	1500	2000	355	285	70	98	2
P4	−2800	10	800	425	124.6	450	1800	1800	458	432	26	96	3
P5	−2800	10	800	510	126.6	530	1800	1800	548	517	31	95	4
P6	−2800	30	800	425	128	500	1800	1800	520	432	88	98	2

for our study. The parameter M_2 is set to 900 GeV. The trilinear couplings with the exception of A_t are all set to zero. The pseudoscalar mass m_A is set to 500 GeV. All the benchmark points have been checked against the constraints mentioned in Sec. II B.

III. SIGNAL AND BACKGROUND

We simulate the collider signatures of the stop pair production [Eq. (4)] for the benchmark points as shown in Tables I and II in the dijet $+ \not{p}_T$ scenario and the corresponding SM background at the LHC. As pointed out earlier, the final state objects like jets and $\not{p}_T$ are expected to be soft because of low Δm making it difficult to obtain a reasonable acceptance after cuts necessary to suppress the SM backgrounds. The signal cross section is rather small at 8 TeV and falls to $\sim$50 fb for a stop mass of 500 GeV. Most of the search strategies proposed have taken recourse to monojet $+ \not{p}_T$ or monophoton $+ \not{p}_T$ searches, where a hard QCD jet is used along with a large $\not{p}_T$ [59]. It was demonstrated in [59] that with this strategy it is possible to use this channel for stop discovery, for stop masses up to $\sim$300 GeV at 14 TeV LHC, with 100 fb^{-1} luminosity.

Corresponding to the signal the principal SM backgrounds that can mimic the signal process are as follows.

(i) *QCD*: The final state is swamped by the QCD dijet events, since the QCD cross section at hadron colliders is enormous. The $\not{p}_T$ source in this case comes from semileptonic B decays. There are nonphysics sources due to mismeasurement of jets and detector noise, which are out of the scope of this study.

(ii) **z**($\rightarrow \nu\bar{\nu}$)+jets: This makes up the irreducible part of our background that looks exactly like the signal. Although the principal part of this background is $Z +$ 2 jets, contribution from higher jet multiplicities are not negligible if some of the jets are not identified.

(iii) **w**($\rightarrow l\bar{\nu}$) + jets: This process contributes dominantly to the background when the lepton is not identified. Since the cross section for W + jets is rather large this also contributes significantly to the background.

(iv) $t\bar{t}$: This is primarily dominant when either the leptons from the W decay and/or some of the final state jets are not identified leading to the same configuration as the signal.

(v) **WW**: This process contributes to the background when one W decays hadronically while the other leptonically.

(vi) **WZ**: This again contributes substantially to the background when W decays leptonically and Z decays hadronically with the lepton not being identified, or when Z decays to $\nu\bar{\nu}$ and W hadronically.

(vii) **ZZ**: This irreducible background mimics the signal in the situation Z($\rightarrow \nu\bar{\nu}$)Z($\rightarrow q\bar{q}$).

We simulate the signal and the background processes $t\bar{t}$, WW, WZ, ZZ using PYTHIA6 [104]. For the background processes W/Z + jets, parton level events are generated using ALPGEN [105] and subsequently passed on to PYTHIA6 for showering and hadronization. Jets are reconstructed using FastJet [106] with an anti-k$_T$ [107] algorithm setting a size parameter R = 0.5. Jets are selected with the following criteria:

$$p_T^j \geq 30(60) \text{ GeV} \quad \forall \ 8(13) \text{ TeV}, \quad |\eta| \leq 3. \quad (8)$$

MLM matching [108] is performed while showering parton level events using PYTHIA for W/Z + jets with a matching cone of $\Delta R = 0.7$ and a jet p_T threshold of 30 GeV within $|\eta| \leq 2.5$. We use CTEQ6L [109] as a parton density function from the LHAPDF [110] package and set $Q^2 = \hat{s}$. Leptons are selected with

$$p_T^l \geq 10 \text{ GeV}, \quad |\eta| \leq 2.5, \quad (9)$$

which are used to veto events.

In order to suppress these backgrounds, in particular the large QCD dijet background, we use the kinematic variable,

$$\alpha_T = p_T^{j_2}/m_T^{jj}, \quad (10)$$

where $p_T^{j_2}$ is the transverse momentum of the second hardest jet and m_T^{jj} is the transverse mass of the two-jet system [111]. It can be observed that for pure dijet events, without any hard $\not{p}_T$ like QCD, the jets are back to back in the transverse plane. Therefore the minimum value of m_T^{jj} in the limit when jet masses can be ignored turns out to be $2p_T^j$ and thus the distribution of α_T has a sharp end point at 0.5. However for dijet events in association with a significant amount of $\not{p}_T$, as is the case for the signal in
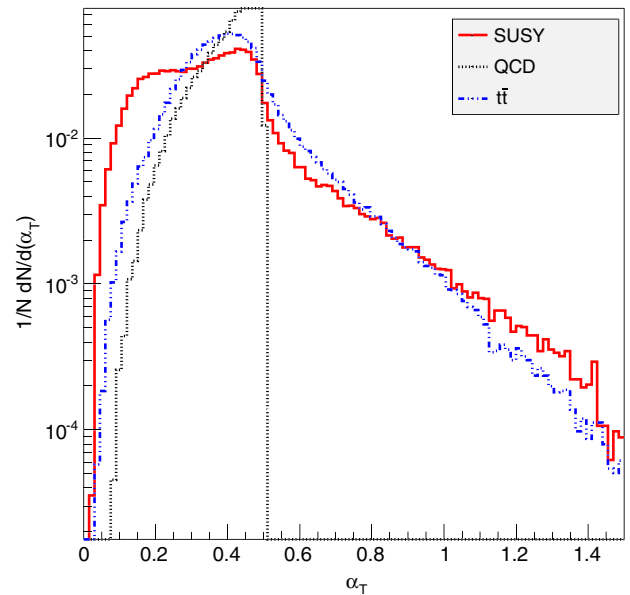
FIG. 3 (color online). α_T distribution for signal and background at 8 TeV LHC energy. The signal corresponds to P2 from Table I. The number of events generated correspond to the fourth column in Table III.

TABLE III. The cross sections (fb) for signal and backgrounds after each cut for 8 TeV LHC energy. The last two columns present normalized cross sections (fb) after all cuts without and with identification of c-like jets respectively. All energy units are in GeV.

Proc	$m_{\tilde{t}_1}, m_{\chi_1^0}$ GeV	CS	N	LJV + 2J + bJV	$\alpha_T \geq 0.55$	$M_{T2} \geq 130$	$\frac{\not{p}_T}{H_T} \leq 0.9$	CS (c-like)
P1	241,198	6330	0.5 M	1996.2	262.3	4.7	2.1	0.45
P2	331,306	1060	0.5 M	227.4	28.1	2.3	0.9	0.1
P3	355,285	700	0.5 M	262	46	0.6	0.25	0.12
P4	458,432	150	0.5 M	33.1	4.2	0.3	0.14	0.01
P5	548,517	45	0.5 M	11.5	1.42	0.1	0.04	0.007
P6	520,432	63	0.5 M	23.5	4.1	0.085	0.04	0.02
$t\bar{t} - 5 - 200$		85000	2 M	6063.4	80.24	8.9	0.46	0.17
$t\bar{t} - 200 - 500$		9500	0.5 M	13.9	3.9	1.5	0.38	1
$t\bar{t} - 500 - \infty$		130	0.5 M	2.1	0.005	0.003	0.003	<1
qcd-300-500		1.3×10^6	3 M	37512.7	<1	<1	<1	<1
WW		35000	0.5 M	7462.2	380.2	2.94	0.84	0.14
WZ		13000	0.5 M	2547.8	189.3	3.1	0.76	0.21
ZZ		5400	0.5 M	1050.1	78.12	1.62	0.3	0.02
$Z(\rightarrow \nu\bar{\nu}) + 2\ jets$		10^5	320910	71215.2	6877.4	67.07	29.4	<1
$Z(\rightarrow \nu\bar{\nu}) + 3\ jets$		16500	241202	5349.6	637.0	9.9	4.5	0.13
$Z(\rightarrow \nu\bar{\nu}) + 4\ jets$		4240	39203	361.4	41.3	0.75	0.6	<1
$W(\rightarrow l\nu) + 2\ jets$		5.8×10^5	565087	117335.6	10752.1	63.4	35.3	2.1
$W(\rightarrow l\nu) + 3\ jets$		10^5	364287	14100.0	1240.8	9.1	6.1	<1
$W(\rightarrow l\nu) + 4\ jets$		16300	44238	785.6	68.9	1.5	1.1	<1

Eq. (4), the two jets are not back to back, leading to large values of α_T. We present the α_T distribution for signal and background in Fig. 3 subject to the jet selection cuts [Eq. (8)] along with lepton veto. The signal process is for P2 in Table I with $m_{\tilde{t}_1}, m_{\chi_1^0}$ masses of 331 and 306 GeV respectively. The number of events generated to construct these plots correspond to the fourth column in Table III (8 TeV). It can be seen in the figure, that as predicted, the QCD process has a sharp fall at ≈ 0.5 and therefore we impose a selection cut [111],

$$\alpha_T > 0.55. \qquad (11)$$

In addition we also use the kinematic variable M_{T2} [112,113] defined as

$$M_{T2}(j_1, j_2, \not{p}_T) = min[max\{M_T(j_1, \chi), M_T(j_2, \chi)\}], \qquad (12)$$

the minimization being performed over $\not{p}_T^{\ 1} + \not{p}_T^{\ 2} = \not{p}_T$ where $\not{p}_T^{\ 1}$, $\not{p}_T^{\ 2}$ are all possible partitions of invisible transverse momentum ($\not{p}_T$), which is due to the presence of LSP for signal and neutrinos for SM backgrounds. Here χ is the invisible particle whose mass (M_χ) is an unknown parameter. The kinematic variable transverse mass (M_T) between the jet and the accompanying missing particle is

$$M_T^2 = M_j^2 + M_\chi^2 + 2(E_T^j E_T^\chi - \vec{p}_T^{\ j} \cdot \vec{p}_T^{\ \chi}), \qquad (13)$$

where $\vec{p}_T^{\ j}$ is the transverse momentum vector of the jet and E_T^j the corresponding energy, while $\vec{p}_T^{\ \chi}$ is the missing transverse momentum ($\not{p}_T$) vector.

Since the maximum value of M_T is restricted to the mass of the parent particle, M_{T2} is also expected to be bounded by the respective parent particle mass. Here M_{T2} is calculated by setting $M_\chi = 0$ without any loss of generality [114]. This assumption is clearly valid for SM processes where the missing momentum is mainly due to neutrinos. Furthermore, we found no significant difference to the population of events near the end points for the signal with massive χ when we make this assumption. However, there may be a difference in acceptance for the two cases which we will consider as a systematic uncertainty in the acceptance efficiency. In the SUSY processes where the parent particle ($\tilde{t}_1$) is heavier than SM particles, the tail in the M_{T2} distribution is expected to extend up to a larger value. This variable thus provides an excellent handle to suppress the remainder of the background rates.

In Fig. 4, the signal and background distributions for M_{T2} are displayed for 8 (left) and 13 (right) TeV LHC energies. The distribution is subject to a dijet criteria along with a lepton veto with jet and lepton selection criteria [Eqs. (8) and (9)]. The signal distribution displayed in the figure corresponds to the benchmark P2 in Table I. The number of events generated to construct these plots corresponds to the fourth column in Tables III (8 TeV) and IV (13 TeV).

We observe that for the signal process at 8 TeV the tail extends beyond the background processes and further reaches beyond the stop mass while for the background the end point of the distributions corresponds to lower values of M_{T2}. As the missing energy in Z + jets comes from Z decaying to a pair of neutrinos from the same side of the configuration, the M_{T2} distribution is not expected to have an end point at the Z mass which is reflected in this plot
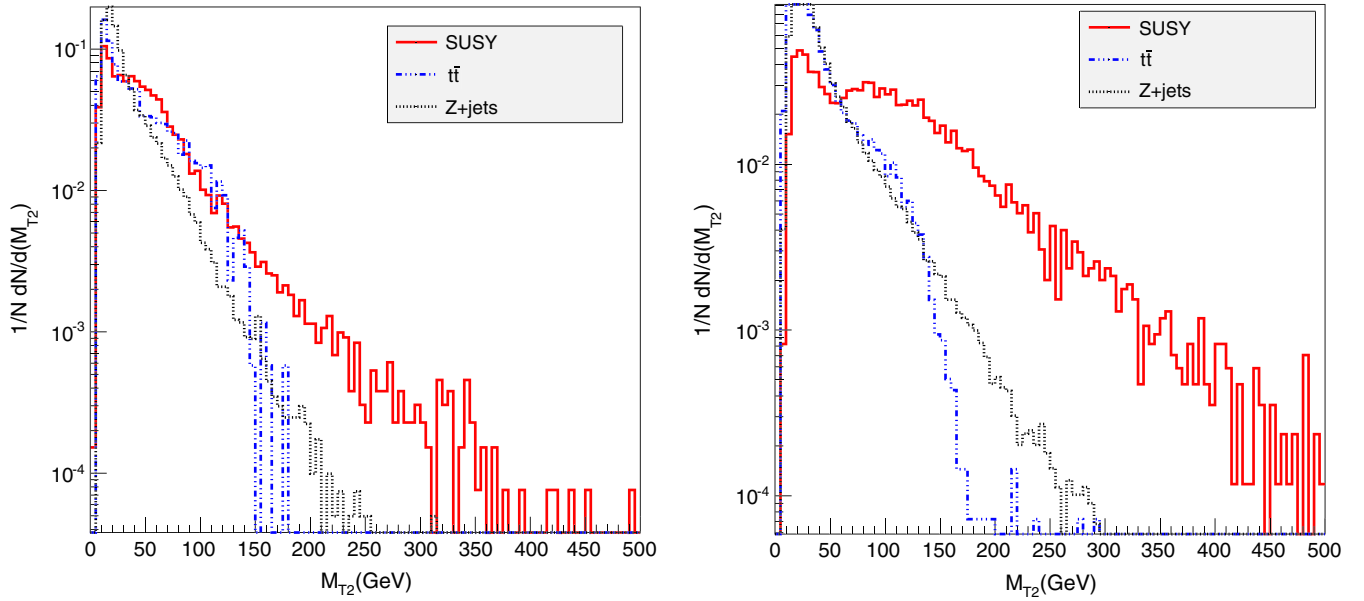
FIG. 4 (color online). M_{T_2} distribution for signal and background for 8 TeV (left) and 13 TeV (right). The signal corresponds to P2 in Table I. The number of events generated corresponds to the fourth column in Tables III (8 TeV) and IV (13 TeV).

[114]. In the case of a $t\bar{t}$ background and the signal also, the distribution extends beyond the expected end point at the parent particle mass. The contribution of events in this region is dominantly due to the jets from hard radiations, in particular from final state radiations [114]. This phenomenon is more evident at 13 TeV energy where objects are kinematically heavily boosted. By observing the distributions, we apply a cut at

$$M_{T2} > 130 \text{ GeV}(250 \text{ GeV}) \quad \text{for } 8(13) \text{ TeV.} \quad (14)$$

This fact can be exploited to suppress backgrounds when the signal is in unfavorable condition kinematically (e.g. for small Δm). For example, for very small Δm, $\tilde{t}_1$ mostly decays invisibly, and hence M_{T2} constructed out of this hard $\not{p}_T$ and jets originating from initial and final state radiation (ISR/FSR) which are uncorrelated with the $\not{p}_T$ has a much larger tail. For larger values of Δm, the longer tail is not observed due to the fact that $\tilde{t}_1$ will have both visible and the invisible (LSPs) decay products for which the momenta are correlated. In Fig. 5 we present the

TABLE IV. Same as Table III but for 13 TeV LHC.

Proc	$m_{\tilde{t}_1}, m_{\chi_1^0}$ GeV	CS	N	LJV + 2J + bJV	$\alpha_T \geq 0.55$	$M_{T2} \geq 250$	$\frac{\not{p}_T}{H_T} \leq 0.9$	CS (c-like)
P1	241,198	24100	0.5 M	3113.2	311.6	8.1	4.4	0.45
P2	331,306	4800	0.5 M	440.2	82.0	5.8	3.2	0.18
P3	355,285	3280	0.5 M	725.5	83.27	1.95	0.7	0.14
P4	458,432	820	0.5 M	84.7	16.8	1.63	0.75	0.03
P5	548,517	290	0.5 M	34.2	6.2	0.5	0.29	0.023
P6	520,432	400	0.5 M	121	17.8	0.29	0.1	0.04
$t\bar{t} - 5 - 200$		291,000	4 M	18690.2	2011.1	0.15	0.15	<1
$t\bar{t} - 200 - 500$		39800	0.5 M	492.2	85.2	<1	<1	<1
$t\bar{t} - 500 - \infty$		900	0.5 M	12.4	0.13	<1	<1	<1
WW		69800	1 M	11858.3	376.2	0.14	<1	<1
WZ		26300	1 M	4144.9	231.5	0.5	0.15	<1
ZZ		10900	1 M	1812.6	128.9	0.46	0.06	<1
$Z(\to \nu\bar{\nu}) + 2\ jets$		241,800	2,605,885	34572.5	2643.4	12.4	1.3	<1
$Z(\to \nu\bar{\nu}) + 3\ jets$		48000	418,467	14282.9	115.9	3.15	0.45	<1
$Z(\to \nu\bar{\nu}) + 4\ jets$		11200	48473	3477.7	294.1	3.1	0.35	<1
$W(\to l\nu) + 2\ jets$		1,185,000	1,763,283	76017.1	3529.8	8.4	<1	<1
$W(\to l\nu) + 3\ jets$		229,000	476,382	27524.6	1490.2	3.0	<1	<1
$W(\to l\nu) + 4\ jets$		47200	103,178	6278.9	400.1	1.2	<1	<1
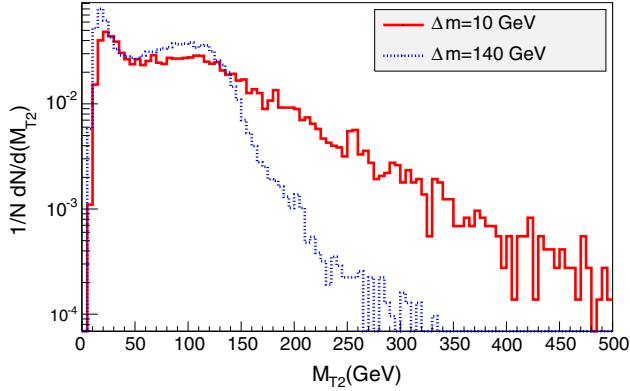
FIG. 5 (color online). M_{T2} distribution for two values of Δm of 10 GeV for solid (red) and 140 GeV for broken (blue) for a $m_{\tilde{t}_1}$ of 240 GeV at 13 TeV LHC energy; 0.5 M events were generated to construct these plots.

distribution for these two cases, with $\Delta m = 10$ and 140 GeV. Clearly M_{T2} gives some handle to recover sensitivity for the low Δm scenario. It is to be noted here also that for the case $\Delta m = 140$ GeV, the decay $\tilde{t}_1 \rightarrow bW\chi_1^0$ may open up, competing with the flavor violating decay mode. Clearly the flavor violating decay mode with very low Δm have some benefits due to ISR/FSR effects. However, it is clear that these effects have a dependence on the models employed in the event generators. Therefore, in order to understand its effect in our signal sensitivity in a more precise manner one needs to do more detailed investigation which is postponed to a future work.

Finally, considering signal and background characteristics, we use the following cuts to suppress the backgrounds.

(i) *Lepton veto (LV)*: In the signal process leptonic activity is absent. However background processes like $t\bar{t}$, W + jets, WW, WZ contain a significant fraction of leptons from W/Z decays accompanied by $\not{p}_T$. The use of lepton veto thus helps to suppress the backgrounds efficiently. Leptons are selected using cuts described in Eq. (8).

(ii) *2 jets (2J)*: We select exclusively dijets with the jet p_T thresholds as described in Eq. (9). Note that after the lepton veto, the $t\bar{t}$ background contribution is expected to be rich in hadronic activity and have more than two jets in the event. Hence a strict imposition of the dijet criteria is expected to reduce the background coming from the $t\bar{t}$, W/Z + jet processes.

(iii) *b-jet veto (bJV)*: This veto is extremely efficient in suppressing the top background. The b-jet identification is implemented by performing a matching of the jets with b quarks assuming a matching cone $\Delta R(b, j) = 0.2$.

(iv) $\alpha_{\mathrm{T}} \geq 0.55$ as discussed in Eq. (11).

(v) $M_{T2} \geq 130$ GeV (250 GeV for 13 TeV) as given by Eq. (14).

(vi) $\not{p}_T/H_T \leq 0.9$: For signal processes we expect this ratio to be less than 1, while in background processes

this is expected to be close to 1. The difference in the azimuthal angle between the two-jet system and the missing energy in the signal and background being primarily responsible for this behavior. We find that this selection is extremely effective in suppressing the $t\bar{t}$ background.

At the end, we explore the possibility of an improvement by somehow tagging charm jets which are a part of the signal. The identification of charm jets is quite challenging. Recently however, attempts have been made to measure the $W + c$ jets cross section where c jets are identified [115]. Note that the channel $\tilde{t}_1 \rightarrow c\chi_1^0$ has been recently searched by ATLAS by trying to identify charm jets in the final state [116]. Although the method we employ is rather simplified, it still points out that charmlike jet identification can prove to be extremely effective in this case. To identify charm jets we match jets with charm quarks, using a matching cone of R = 0.2. To find the presence of charm jets one can further check the presence of a D meson among the jet constituents, which we postpone to a future work.

IV. RESULTS

Simulating the signal and background processes using the selection cuts as described above, we present results for 8 and 13 TeV LHC energies in Tables III and IV respectively. The first four columns present the processes (Proc), the masses of the lightest stop ($m_{\tilde{t}_1}$) and LSP ($m_{\chi_1^0}$), the cross section (CS), and the number of events generated (N) for each process respectively. We compute the next-to-leading-order signal cross section using PROSPINO [117]. The subsequent columns display the cumulative effects of cuts, as normalized cross sections (production cross section multiplied by cut efficiency). In the penultimate column the cross sections after all cuts are presented. The top and the QCD backgrounds are simulated by slicing the entire phase space into $\hat{p}_T$ bins, where $\hat{p}_T$ is the transverse momenta of the produced partons in the partonic frame. In both tables we notice that the combined effects of lepton veto, b-jet veto and the dijet criteria (LV + 2J + bJV) reduce the top background by an enormous amount ($\sim$95%) while reducing the signal process by about a third. As pointed out earlier, the α_T cut successfully isolates the entire QCD background as expected. For the sake of simplicity we have quoted numbers corresponding to only one $\hat{p}_T$ bin for QCD. The rest of the backgrounds, particularly from top and the WW/WZ/ZZ are also suppressed by a significant amount, costing a significant fraction of signal cross section as well. The M_{T2} cut, as pointed out, removes a substantial fraction of $t\bar{t}$, WW/WZ/ZZ as well as W/Z + jets processes. Clearly the M_{T2} cut plays an important role in isolating backgrounds efficiently. Finally the cut $\not{p}_T/H_T$ suppresses the WW/WZ/ZZ backgrounds and brings it down to a negligible level. Even after a huge suppression of the irreducible backgrounds W/Z + 2, 3 jets, the remaining fraction is

TABLE V.   The signal and backgrounds cross sections for benchmark points. The signal significances ($S/\sqrt{B}$) for different energies and luminosities are also shown.

	P1	P2	P3	P4	P5	P6	Total Backgrounds
$m_{\tilde{t}_1}, m_{\tilde{\chi}_1^0}$ (GeV)	241,198	331,306	355,285	458,432	548,517	520,432	
8 TeV	2.1	0.9	0.25	0.14	0.04	0.04	70.6
$S/\sqrt{B}$(20 fb^{-1})	1.1	0.5	0.13	0.07	0.02	0.02	
13 TeV	4.4	3.2	0.7	0.75	0.29	0.1	2.6
$S/\sqrt{B}$(30 fb^{-1})	15	11	2.4	2.5	1	0.3	

non-negligible because of the large production cross section. Note that even after suppressing the SM backgrounds substantially, since the signal cross section is miniscule, the prospects of discovering a signal at 8 TeV LHC is very limited. In the last column cross sections are presented requiring that out of the two jets in the final state one is a c-like jet. As mentioned earlier, c-like jets are identified by naively matching partonic c quarks and reconstructed jets. Clearly, it shows that identification of c-like jets does help in reducing the background to a large extent. This happens as the signal is likely to have a larger fraction of identified charm jets than the background.

At 13 TeV the results improve significantly as can be seen from Table IV. The larger stop pair production cross section significantly helps in enhancing the event rates. On the other hand an increased boost in the system helps to effectively use the M_{T2} variable by applying a much larger cut value of 250 GeV to isolate the backgrounds. As can be observed from the right panel of Fig. 4, a cut of 250 GeV is extremely effective in suppressing the irreducible $Z +$ jets background. We observe from the last column of Table IV that at 13 TeV energy, the signal and background cross sections are comparable as compared to 8 TeV where the background cross sections are dominant.

Table V summarizes cross sections of the signal and background after all cuts for 8 and 13 TeV LHC energy. The $t\bar{t}$ cross section has been multiplied in the table by a k factor of 2 to take into account next-to-leading-order effects [118]. Note that the k factors for W/Z + jets processes are very close to 1 [119,120], and hence do not change our results significantly. From Table V we find that at 8 TeV the total background is 70.6 fb in which the dominant contribution comes from W/Z + jets, while the signal cross section varies from 2.1 fb for P1 to 0.04 fb in P6. Therefore for P1 with 20 fb^{-1} luminosity we obtain $S/\sqrt{B} = 1.1$, while the significance drops substantially with the increase of $m_{\tilde{t}_1}$. At 13 TeV the total background cross section turns out to be 2.6 fb while the signal cross section varies from 4.4 fb in P1 to 0.1 fb in P6. Thus for the points P1 and P2 we obtain $S/\sqrt{B} = 6.1$ and 4.4 respectively for 5 fb^{-1} which implies that P1 is discoverable while an evidence of a signal can be obtained even with low luminosity options for P2. With 100 fb^{-1} luminosity we find that the benchmarks P3 and P4 have significance values of 4.7 and 4.3 respectively.

With this strategy we attempt to explore the sensitivity in Δm for various values of $m_{\tilde{t}_1}$ at a given luminosity. We present our findings in Fig. 6 where the accessible region below the curves are shown in the $m_{\tilde{t}_1} - \Delta m$ plane for two luminosity options 5 and 100 fb^{-1} with $S\sqrt{B} \geq 5$. This plot is presented with the assumption of $BR(\tilde{t}_1 \to c\chi_1^0) = 100\%$ holding the rest of the parameters fixed as described in Sec. II. The plot is obtained by a parameter space scan in the $m_{\tilde{t}_1} - \Delta m$ plane with a grid spacing of 20 GeV on the $m_{\tilde{t}_1}$ (X) axis and 5 GeV on the Δm (Y) axis. We find that even for low luminosity a light stop up to a mass of ~350 GeV could be explored for $\Delta m = 20$ GeV. As mentioned earlier this search strategy is very sensitive to lower values of Δm and it is reflected in the figure. For a luminosity of 100 fb^{-1} we find that a light stop up to a mass of 450 GeV can be probed for Δm as low as 35 GeV. The solid horizontal line demarcates the kinematic region $m_{\tilde{t}_1} < m_t + m_{\chi_1^0}$, over which the the decay $\tilde{t}_1 \to t\chi_1^0$ opens up and dominates.
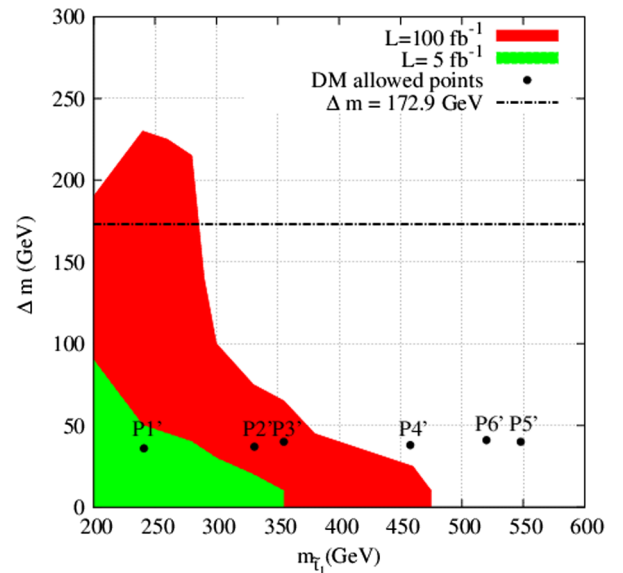
FIG. 6 (color online).   The 5σ significance contours for $\mathcal{L} = 5$ fb^{-1} {green(light solid)}, and for $\mathcal{L} = 100\ fb^{-1}$ {red(dark solid)} luminosity assuming $\tilde{t}_1 \to c\chi_1^0$ to be 100% for 13 TeV LHC energy. The black (broken) line corresponds to $m_t = 172.9$ GeV and is the kinematic limit for $\tilde{t}_1 \to t + \chi_1^0$. The dark matter allowed points P1'—P6' corresponding to Table VI are denoted by the black (solid) dots.

TABLE VI.   Relic density for the benchmarks P1—P6 and the modified benchmarks P1'—P6'.

	P1	P2	P3	P4	P5	P6
$m_{\tilde{t}_1}, m_{\tilde{\chi}_1^0}$ (GeV)	241,198	331,306	355,285	458,432	548,517	520,432
Ωh^2	0.17	0.04	1.9	0.04	0.06	0.59
	P1'	P2'	P3'	P4'	P5'	P6'
$m_{\tilde{t}_1}, m_{\tilde{\chi}_1^0}$ (GeV)	241,205	331,294	355,315	458,420	548,508	520,479
Ωh^2	0.119	0.119	0.119	0.119	0.119	0.119
Δm (GeV)	36	37	40	38	40	41

A. Implications for dark matter

In scenarios with a small stop-neutralino mass splitting and a bino ($\tilde{B}$) LSP, stop coannihilation can play an important role in determining the relic dark matter abundance. This is the case especially for small Δm, i.e., where the decay $\tilde{t}_1 \to c\tilde{\chi}_1^0$ is dominant. Hence it is important to investigate the implications of our studies for probing the stop-coannihilation scenario at the LHC.

The relic density crucially depends on the stop-neutralino mass difference as well as on other parameters that will be discussed in the next paragraph. For the benchmarks considered, the value of the relic density as shown in Table VI is either above (P1,P3,P6) or below (P2,P4,P5) the central value for Planck, $\Omega_{\mathrm{DM}} h^2 = 0.1199$ [121]. However it is well known that the value of the relic density in coannihilation scenarios depends critically on the NLSP-LSP mass difference, hence a small decrease (increase) in the stop-neutralino mass difference will lead to a large decrease (increase) in the value of the relic density.. We have therefore searched for modified benchmarks for which the relic density was in agreement with the central value of Planck. For this, we vary only the mass of the lightest neutralino by changing M_1, while keeping all other parameters of each benchmark P1—P6 to their value at the electroweak symmetry breaking (EWSB) scale. The modified benchmarks, P1'—P6', with the corresponding stop and neutralino masses are listed in Table IV. The relic density is calculated using micrOMEGAs3 [122]. Furthermore, their position in the $\Delta m - m_{\tilde{t}_1}$ plane is displayed in Fig. 6. We find that for the benchmark points that satisfy the Planck constraint our search strategy works very well indeed. We achieve reasonable sensitivity for stop masses below 400 GeV with an integrated luminosity $\mathcal{L} = 100$ fb^{-1} at 13 TeV LHC as can be seen in Fig. 6. In fact the 5σ significance contours for $L = 5$ fb^{-1} even covers the relevant Δm for stop masses below 280 GeV.

A few comments are in order to ascertain the generality of this result since the relic density depends not only on the stop-neutralino mass difference but also on the nature of the neutralino LSP, the nature of $\tilde{t}_1$ (whether it is dominantly left handed (LH) or right handed (RH), and on the value of M_A. First note that the mass splittings associated with the modified benchmarks of Table VI are typical of scenarios where the LSP is a bino, and these are precisely the ones

where stop coannihilation plays an important role in obtaining a low enough relic density. Second, the mass splitting required to satisfy the Planck constraint—for a given stop mass—should depend on whether the stop is LH (P3'—P6') or RH (P1' and P2'). The reason is the following: coannihilation processes such as $\tilde{\chi}_1\tilde{t}_1 \to tg$, th have a larger cross section for a RH stop than for a LH stop of the same mass since the coupling to the bino LSP is proportional to the top hypercharge (which is larger for the RH top/stop), hence one would expect the required Δm to be larger for a RH stop. Furthermore the QCD processes involving pairs of squarks $\tilde{t}_1\tilde{t}_1 \to tt$, $\tilde{t}_1\tilde{b}_1 \to tb$... which are more important for LH stops involve two Boltzmann suppression factors,[2] therefore the mass splitting required is smaller. However since the Boltzmann factor varies rapidly with Δm, in the end there is only a few GeV difference between the case of the RH and LH stop. For example for benchmark P2', the required mass splitting would be $\Delta m = 29$ GeV for a dominantly LH stop instead of $\Delta m = 37$ GeV for a RH one. Finally, the pseudoscalar mass M_A can also be a relevant parameter. For P1' and P2' it is set by CMSSM boundary conditions and is rather high hence plays no role in neutralino annihilation while for P3'—P6', it is set to 500 GeV. A higher value of M_A would not affect our collider search strategy and the relevant branching ratios of $\tilde{t}_1 \to c\tilde{\chi}_1^0$. However it would imply smaller mass differences than the ones listed in Table VI, and hence would easily be covered by our search strategy. We can therefore safely conclude that the channel investigated here can probe the stop-coannihilation scenario for stop masses up to at least 400 GeV.

V. CONCLUSION

In this study we perform a comprehensive analysis of the collider search prospects of the flavor violating decay of the stop quark, namely $\tilde{t}_1 \to c\tilde{\chi}_1^0$. Such a scenario is well motivated in the context of natural SUSY as well as from the dark matter perspective of stop coannihilation. It had been earlier observed that this channel is rather difficult to probe due to the low mass difference between the stop quark and the lightest neutralino. The principle

---

[2]The Boltzmann factor is $e^{-\Delta m/T_f}$ for each coannihilating particle and T_f is the freeze-out temperature.

background to this channel arises from QCD, $t\bar{t}$ and $z(\nu\bar{\nu})/W(\to l\nu)$ + jets final state. We use the kinematic variables α_T and M_{T2} to effectively suppress these at 8 and 13 TeV LHC. At 8 TeV, the level of background is still high and we are limited by low stop pair production cross section. We find that our strategy is far more effective at 13 TeV due to the increase in cross section and efficient use of the kinematic variables. We observe that it is possible to discover light stop quarks up to a mass of $\sim$450 GeV with 100 fb^{-1} luminosity at 13 TeV LHC energy for low values of Δm and even for the case when the $\tilde{t}_1$ and χ_1^0 are almost degenerate. We observe that for the very low Δm case, the loss of acceptance because of soft visible particles in the final states is compensated by ISR/FSR effects through M_{T2} selection. The result improves significantly when one attempts identifying charm jets both at 8 and 13 TeV LHC. We also show the discoverable region in the $m_{\tilde{t}_1} - \Delta m$ plane assuming the branching ratio of $\tilde{t}_1 \to c\chi_1^0$ to be 100% This is useful information in the context of dark matter via stop coannihilation. Our analysis shows that a good region of the parameter space relevant for the stop-coannihilation scenario can be probed at 13 TeV LHC energy.

[1] S. Chatrchyan *et al.* (CMS Collaboration), Phys. Lett. B **716**, 30 (2012).

[2] G. Aad *et al.* (ATLAS Collaboration), Phys. Lett. B **716**, 1 (2012).

[3] H. Baer, V. Barger, and A. Mustafayev, Phys. Rev. D **85**, 075010 (2012).

[4] S. Akula, B. Altunkaynak, D. Feldman, P. Nath, and G. Peim, Phys. Rev. D **85**, 075001 (2012).

[5] J. L. Feng, K. T. Matchev, and D. Sanford, Phys. Rev. D **85**, 075007 (2012).

[6] S. Heinemeyer, O. Stal, and G. Weiglein, Phys. Lett. B **710**, 201 (2012).

[7] O. Buchmueller, R. Cavanaugh, A. De Roeck, M. Dolan, J. Ellis *et al.*, Eur. Phys. J. C **72**, 2020 (2012).

[8] P. Draper, P. Meade, M. Reece, and D. Shih, Phys. Rev. D **85**, 095007 (2012).

[9] J. Cao, Z. Heng, D. Li, and J. M. Yang, Phys. Lett. B **710**, 665 (2012).

[10] L. J. Hall, D. Pinner, and J. T. Ruderman, J. High Energy Phys. 04 (**2012**) 131.

[11] J. Ellis and K. A. Olive, Eur. Phys. J. C **72**, 2005 (2012).

[12] H. Baer, V. Barger, and A. Mustafayev, J. High Energy Phys. 05 (**2012**) 091.

[13] L. Maiani, A. Polosa, and V. Riquer, New J. Phys. **14**, 073029 (2012).

[14] T. Cheng, J. Li, T. Li, D. V. Nanopoulos, and C. Tong, Eur. Phys. J. C **73**, 2322 (2013).

[15] J.-J. Cao, Z.-X. Heng, J. M. Yang, Y.-M. Zhang, and J.-Y. Zhu, J. High Energy Phys. 03 (**2012**) 086.

[16] F. Brummer, S. Kraml, and S. Kulkarni, J. High Energy Phys. 08 (**2012**) 089.

[17] C. Balazs, A. Buckley, D. Carter, B. Farmer, and M. White, Eur. Phys. J. C **73**, 2563 (2013).

[18] J. L. Feng and D. Sanford, Phys. Rev. D **86**, 055015 (2012).

[19] D. Ghosh, M. Guchait, S. Raychaudhuri, and D. Sengupta, Phys. Rev. D **86**, 055007 (2012).

[20] A. Fowlie, M. Kazana, K. Kowalska, S. Munir, L. Roszkowski, E. M. Sessolo, S. Trojanowski, and Y.-L. S. Tsai, Phys. Rev. D **86**, 075010 (2012).

[21] P. Athron, S. King, D. Miller, S. Moretti, and R. Nevzorov, Phys. Rev. D **86**, 095003 (2012).

[22] M. W. Cahill-Rowley, J. L. Hewett, A. Ismail, and T. G. Rizzo, Phys. Rev. D **86**, 075015 (2012).

[23] S. Akula, P. Nath, and G. Peim, Phys. Lett. B **717**, 188 (2012).

[24] J. Cao, Z. Heng, J. M. Yang, and J. Zhu, J. High Energy Phys. 10 (**2012**) 079.

[25] A. Arbey, M. Battaglia, A. Djouadi, and F. Mahmoudi, J. High Energy Phys. 09 (**2012**) 107.

[26] P. Nath, arXiv:1207.5501.

[27] J. Ellis, F. Luo, K. A. Olive, and P. Sandick, Eur. Phys. J. C **73**, 2403 (2013).

[28] M. Chakraborti, U. Chattopadhyay, and R. M. Godbole, Phys. Rev. D **87**, 035022 (2013).

[29] A. Arbey, M. Battaglia, A. Djouadi, and F. Mahmoudi, Phys. Lett. B **720**, 153 (2013).

[30] A. Chakraborty, B. Das, J. L. Diaz-Cruz, D. K. Ghosh, S. Moretti *et al.*, arXiv:1301.2745.

[31] A. Dighe, D. Ghosh, K. M. Patel, and S. Raychaudhuri, Int. J. Mod. Phys. A **28**, 1350134 (2013).

[32] A. Arbey, A. Deandrea, F. Mahmoudi, and A. Tarhini, Phys. Rev. D **87**, 115020 (2013).

[33] G. Belanger, G. D. La Rochelle, B. Dumont, R. M. Godbole, S. Kraml, and S. Kulkarni, Phys. Lett. B **726,** 773 (2013).

[34] A. Djouadi, L. Maiani, G. Moreau, A. Polosa, J. Quevillon *et al.*, arXiv:1307.5205.

[35] R. M. Chatterjee, M. Guchait, and D. Sengupta, Phys. Rev. D **86,** 075014 (2012).

[36] K. Howe and P. Saraswat, J. High Energy Phys. 10 (**2012**) 065.

[37] A. Arbey, M. Battaglia, and F. Mahmoudi, arXiv:1212.6865.

[38] H. Baer, V. Barger, A. Lessa, and X. Tata, Phys. Rev. D **86,** 117701 (2012).

[39] CERN Report No. CMS-PAS-SUS-12-005, 2012.

[40] CERN Report No. ATLAS-CONF-2012-109, 2012.

[41] E. Cremmer, B. Julia, J. Scherk, P. van Nieuwenhuizen, S. Ferrara, and L. Girardello, Phys. Lett. **79B,** 231 (1978).

[42] E. Cremmer, B. Julia, J. Scherk, S. Ferrara, L. Girardello, and P. van Nieuwenhuizen, Nucl. Phys. **B147,** 105 (1979).

[43] A. H. Chamseddine, R. Arnowitt, and P. Nath, Phys. Rev. Lett. **49,** 970 (1982).

[44] L. Hall, J. Lykken, and S. Weinberg, Phys. Rev. D **27,** 2359 (1983).

[45] P. Nath, R. Arnowitt, and A. Chamseddine, Nucl. Phys. **B227,** 121 (1983).

[46] N. Ohta, Prog. Theor. Phys. **70,** 542 (1983).

[47] G. Aad *et al.* (ATLAS Collaboration), J. High Energy Phys. 10 (**2013**) 130.

[48] CERN Report No. ATLAS-CONF-2013-047, 2013.

[49] CERN Report No. ATLAS-CONF-2013-061, 2013.

[50] A. G. Cohen, D. Kaplan, and A. Nelson, Phys. Lett. B **388,** 588 (1996).

[51] J. Berger, J. Hubisz, and M. Perelstein, J. High Energy Phys. 07 (**2012**) 016.

[52] J. Cao, C. Han, L. Wu, J. M. Yang, and Y. Zhang, J. High Energy Phys. 11 (**2012**) 039.

[53] L. Randall and M. Reece, J. High Energy Phys. 08 (**2013**) 088.

[54] J. R. Espinosa, C. Grojean, V. Sanz, and M. Trott, J. High Energy Phys. 12 (**2012**) 077.

[55] H. Baer, V. Barger, P. Huang, D. Mickelson, A. Mustafayev, and X. Tata, Phys. Rev. D **87,** 035017 (2013).

[56] M. Papucci, J. T. Ruderman, and A. Weiler, J. High Energy Phys. 09 (**2012**) 035.

[57] N. Desai and B. Mukhopadhyaya, J. High Energy Phys. 05 (**2012**) 057.

[58] B. He, T. Li, and Q. Shafi, J. High Energy Phys. 05 (**2012**) 148.

[59] M. Drees, M. Hanussek, and J. S. Kim, Phys. Rev. D **86,** 035024 (2012).

[60] T. Plehn, M. Spannowsky, and M. Takeuchi, J. High Energy Phys. 08 (**2012**) 091.

[61] Z. Han, A. Katz, D. Krohn, and M. Reece, J. High Energy Phys. 08 (**2012**) 083.

[62] V. Barger, P. Huang, M. Ishida, and W.-Y. Keung, Phys. Lett. B **718,** 1024 (2013).

[63] A. Choudhury and A. Datta, Mod. Phys. Lett. A **27,** 1250188 (2012).

[64] C. -Y. Chen, A. Freitas, T. Han, and K. S. Lee, J. High Energy Phys. 11 (**2012**) 124.

[65] S. Bornhauser, M. Drees, S. Grab, and J. Kim, Phys. Rev. D **83,** 035008 (2011).

[66] S. Kraml and A. Raklev, Phys. Rev. D **73,** 075002 (2006).

[67] Z.-H. Yu, X.-J. Bi, Q.-S. Yan, and P.-F. Yin, Phys. Rev. D **87,** 055007 (2013).

[68] M. A. Ajaib, T. Li, and Q. Shafi, Phys. Rev. D **85,** 055021 (2012).

[69] K. Ghosh, K. Huitu, J. Laamanen, and L. Leinonen, Phys. Rev. Lett. **110,** 141801 (2013).

[70] B. Dutta, T. Kamon, N. Kolev, K. Sinha, and K. Wang, Phys. Rev. D **86,** 075004 (2012).

[71] D. S. Alves, M. R. Buckley, P. J. Fox, J. D. Lykken, and C.-T. Yu, Phys. Rev. D **87,** 035016 (2013).

[72] D. Berenstein, T. Liu, and E. Perkins, Phys. Rev. D **87,** 115004 (2013).

[73] D. Ghosh and D. Sengupta, Eur. Phys. J. C **73,** 2342 (2013).

[74] A. Chakraborty, D. K. Ghosh, D. Ghosh, and D. Sengupta, J. High Energy Phys. 10 (**2013**) 122.

[75] D. Ghosh, arXiv:1308.0320 [Phys. Rev. D (to be published)].

[76] C. Han, K.-i. Hikasa, L. Wu, J. M. Yang, and Y. Zhang, J. High Energy Phys. 10 (**2013**) 216.

[77] O. Buchmueller and J. Marrouche, arXiv:1304.2185.

[78] G. D. Kribs, A. Martin, and A. Menon, Phys. Rev. D **88,** 035025 (2013).

[79] K. Kowalska and E. M. Sessolo, Phys. Rev. D **88,** 075001 (2013).

[80] D. E. Kaplan, K. Rehermann, and D. Stolarski, J. High Energy Phys. 07 (**2012**) 119.

[81] T. Plehn, M. Spannowsky, and M. Takeuchi, Phys. Rev. D **85,** 034029 (2012).

[82] CERN Report No. ATLAS-CONF-2012-166, 2012.

[83] CERN Report No. ATLAS-CONF-2013-001, 2013.

[84] CERN Report No. ATLAS-CONF-2012-167, 2012.

[85] "Search for direct top squark pair production in events with a single isolated lepton, jets and missing transverse energy at sqrt(s) = 8 tev".

[86] K.-i. Hikasa and M. Kobayashi, Phys. Rev. D **36,** 724 (1987).

[87] M. Muhlleitner and E. Popenda, J. High Energy Phys. 04 (**2011**) 095.

[88] C. Boehm, A. Djouadi, and Y. Mambrini, Phys. Rev. D **61,** 095006 (2000).

[89] A. Djouadi, M. Guchait, and Y. Mambrini, Phys. Rev. D **64,** 095014 (2001).

[90] S. P. Das, A. Datta, and M. Guchait, Phys. Rev. D **65,** 095006 (2002).

[91] M. Carena, A. Freitas, and C. Wagner, J. High Energy Phys. 10 (**2008**) 109.

[92] G. Belanger, M. Heikinheimo, and V. Sanz, J. High Energy Phys. 08 (**2012**) 151.

[93] CERN Report No. ATLAS-CONF-2011-096, 2011.

[94] S. Chatrchyan *et al.* (CMS Collaboration), J. High Energy Phys. 09 (**2012**) 094.

[95] A. Djouadi *et al.* (MSSM Working Group Collaboration), arXiv:hep-ph/9901246.

[96] A. Djouadi, J.-L. Kneur, and G. Moultaka, Comput. Phys. Commun. **176,** 426 (2007).

[97] F. Mahmoudi, Comput. Phys. Commun. **178,** 745 (2008).

[98] D. Asner *et al.* (Heavy Flavor Averaging Group Collaboration), arXiv:1010.1589.

[99] Y. Amhis *et al.* (Heavy Flavor Averaging Group), arXiv:1207.1158.

[100] A. J. Buras and J. Girrbach, arXiv:1306.3775.

[101] J. R. Ellis, S. Heinemeyer, K. Olive, A. Weber, and G. Weiglein, J. High Energy Phys. 08 (**2007**) 083.

[102] R. Aaij *et al.* (LHCb Collaboration), Phys. Rev. Lett. **111**, 101805 (2013).

[103] S. Chatrchyan *et al.* (CMS Collaboration), Phys. Rev. Lett. **111**, 101804 (2013).

[104] T. Sjostrand, S. Mrenna, and P. Z. Skands, J. High Energy Phys. 05 (**2006**) 026.

[105] M. L. Mangano, M. Moretti, F. Piccinini, R. Pittau, and A. D. Polosa, J. High Energy Phys. 07 (**2003**) 001.

[106] M. Cacciari, G. P. Salam, and G. Soyez, Eur. Phys. J. C **72**, 1896 (2012).

[107] M. Cacciari, G. P. Salam, and G. Soyez, J. High Energy Phys. 04 (**2008**) 063.

[108] S. Hoeche, F. Krauss, N. Lavesson, L. Lonnblad, M. Mangano *et al.*, arXiv:hep-ph/0602031.

[109] H. L. Lai, J. Huston, S. Kuhlmann, J. Morfin, F. Olness, J. F. Owens, J. Pumplin, and W. K. Tung (CTEQ Collaboration), Eur. Phys. J. C **12**, 375 (2000).

[110] D. Bourilkov, R. C. Group, and M. R. Whalley, arXiv:hep-ph/0605240.

[111] L. Randall and D. Tucker-Smith, Phys. Rev. Lett. **101**, 221803 (2008).

[112] A. Barr, C. Lester, and P. Stephens, J. Phys. G **29**, 2343 (2003).

[113] C. Lester and D. Summers, Phys. Lett. B **463**, 99 (1999).

[114] A. J. Barr and C. Gwenlan, Phys. Rev. D **80**, 074007 (2009).

[115] CERN Report No. CMS-PAS-SMP-12-002, 2013.

[116] CERN Report No. ATLAS-CONF-2013-068, 2013.

[117] W. Beenakker, R. Hopker, and M. Spira, arXiv:hep-ph/9611232.

[118] N. Kidonakis, arXiv:1109.3231.

[119] C. F. Berger, Z. Bern, L. J. Dixon, F. Febres Cordero, D. Forde, T. Gleisberg, H. Ita, D. A. Kosower, and D. Maître, Phys. Rev. Lett. **106**, 092001 (2011).

[120] H. Ita, Z. Bern, L. J. Dixon, F. Febres Cordero, D. A. Kosower, and D. Maître, Phys. Rev. D **85**, 031501 (2012).

[121] P. Ade *et al.* (Planck Collaboration), arXiv:1303.5076.

[122] G. Belanger, F. Boudjema, A. Pukhov, and A. Semenov, arXiv:1305.0237.